Scalar Dispersion in a Two Dimensional Random Flow Field

Meredith M. Metzger
Department of Mechanical Engineering
University of Utah

1   Introduction

Experimental observations of the vertical propagation and decay of near inertial oscillations (NIO) through the oceanic mixed layer has stimulated a desire to understand the effect of NIO activity on mixing processes in the upper ocean. Ocean surface forcing due to the passage of large scale wind events or storms instigates the formation of coherent NIO structures which tend to migrate in a helical trajectory as evident from near surface buoy drifters. Observations also indicate that NIO mixed layer activity eventually decays to background levels approximately 20 days after the initial onset of the storm [1]. A major challenge to oceanographers has been to explain the primary mechanisms responsible for the observed time scales of NIO propagation and decay. Young and Ben Jelloul [2] hypothesized that advective distortion by the geostrophic eddy field decreases the NIO horizontal coherence scale. From a multiple time scale analysis, they formulate a reduced NIO equation linearized about the geostrophic flow. This analysis effectively filters out inertial oscillations allowing focus on the near inertial component of the motion. Their NIO equation combines the effects of advection by the geostrophic velocity, wave dispersion, and refraction due to the geostrophic vorticity. Subsequent work by Balmforth *et al.* [3] investigated results from the NIO equation for the case of a background geostrophic shear flow. The present study extends this work by considering the fundamental properties of the NIO equation for the specific case of linearized NIOs superposed on a two stage random wave model of the background geostrophic eddy field.

We begin the paper with an overview of near inertial oscillations and describe the methodology used to obtain the reduced NIO equation that provides the basis for the present study. We will see that the NIO equation is characterized by a parameter termed the dispersivity, analogous to the diffusivity associated with passive scalar diffusion processes. We then discuss the random wave model used to represent the background geostrophic flow and some fundamental properties associated with this type of model flow. We then study some limiting parameter cases of the governing equation, specifically, zero and infinite dispersivity. We present data from the numerical solution of the governing equation for a range of dispersivity values. Finally, we take a look at the decay of energy in the large scales and conclude with comments on directions for future research.

2 Near Inertial Oscillations (NIO)

Inertial oscillations describe fluid motions arising from a force balance between fluid inertia and Coriolis acceleration. The reduced horizontal momentum equations, in a reference frame rotating with the earth, are

$$u_t - f_o v = 0 \qquad \text{and} \qquad v_t + f_o u = 0. \tag{1}$$

where the subscript t represents partial differentiation with respect to time and $f_o = 2\Omega \sin\theta$ is the inertial frequency with θ and Ω denoting the latitude and the earth's rotation rate, respectively. Throughout the paper, we follow the convention that (u, v) describe the horizontal velocity components in the easterly (x) and northerly (y) directions, respectively, and z refers to the vertical direction. The solution to (1), assuming constant f, is simply $\mathcal{U} = \tilde{\mathcal{U}} e^{-i f_o t}$ where $\mathcal{U} = u + iv$ and $\tilde{\mathcal{U}}$ is the initial velocity. The corresponding particle trajectories, $x + iy = \frac{i\tilde{\mathcal{U}}}{f_o} e^{-i f_o t}$, form closed loops. As a simple model of the passage of a storm front, we assume that at time $t = 0$, an instantaneous, homogeneous wind event occurs thereby exciting the entire horizontal domain to move with a uniform velocity of $\tilde{\mathcal{U}}$. The ensuing motions, described by (1), are referred to as inertial oscillations. Using data from mid latitude ocean buoy drifters [1], estimates of the typical diameter of inertial oscillations is of the order of 5km. In reality, however, (1) only represents the leading order behavior of the flow; and therefore, ensuing motions are actually near inertial oscillations that are more accurately characterized by helical type trajectories and have a finite lifespan in the mixed layer of approximately 20 days.

Note, in the solution of (1), a constant inertial frequency f_o was assumed. This assumption ceases to be valid if a coherent fluid motion spans a large enough horizontal extent; then the latitude difference (and, hence, the change in f_o) between the most northerly and southerly points of the coherent motion can no longer be neglected. For simplicity, we neglect these so-called β effects in the remainder of the paper.

3 Reduced Linearized NIO Equation

The previous work of Young and Ben Jelloul [2] regarding near inertial oscillations provides the basis for the present study. We briefly summarize the relevant points of that work here. We begin by assuming hydrostatic, Boussinesq, inviscid, incompressible flow. The velocity is linearized about the background geostrophic flow which can be written compactly in terms of a streamfunction, $\Psi(x, y, z, t) = P_g/(f_o \rho_o)$ with P_g denoting the geostrophic pressure field and ρ_o, the mean density. Further reduction of the linearized governing equations (not reproduced here) is achieved through a multiple time scale analysis with the requirement that internal waves be nearly inertial. The general dispersion relation for internal waves can be written as $\omega^2 = (N_o^2 \kappa_h^2 + f_o^2 \kappa_v^2)/\kappa^2$ where ω is the oscillation frequency, (κ_h, κ_v) denote the horizontal and vertical wavenumbers, respectively, $\kappa^2 = \kappa_h^2 + \kappa_v^2$, and N_o is the characteristic buoyancy frequency associated with the vertical density stratification of the fluid (for further discussion of internal waves, see Gill [4], pp. 258). We define a small parameter $\epsilon \equiv (N_o \kappa_h)/(f_o \kappa_v)$. Physical estimates of N_o in the North Pacific and North Atlantic indicate $N_o/f_o = \mathcal{O}(10^2)$

[5]. Therefore, in order for $\epsilon \ll 1$, the characteristic vertical wavelengths of the motion must be several orders of magnitude smaller than the characteristic horizontal wavelengths, i.e. $\kappa_v \gg \kappa_h$. This is entirely consistent with our use of the hydrostatic approximation (see Gill[4],pp. 159 for a discussion on the equivalence between longwave and hydrostatic approximations). The internal wave dispersion relation then reduces to $\omega^2 \approx f_o^2(1 + \epsilon^2)$; whereby, inertial oscillations are recovered at leading order. Departures from perfect inertial oscillations become appreciable on the slow time scale $t_s \equiv \epsilon^2 f_o t$.

In the multiple time scale analysis, the complex velocity $\mathcal{U}$ is expanded in powers of ϵ^2 giving $\mathcal{U} = \mathcal{U}_0 + \epsilon^2 \mathcal{U}_2 + \dots$ where the leading order solution $\mathcal{U}_0$ is simply the velocity associated with the inertial oscillations governed by (1). For convenience we write the leading order solution as $\mathcal{U}_0 = M_z(x, y, z, t_s) \, e^{-i f_o t}$ which allows for trivial integration of the incompressibility condition to obtain the leading order vertical velocity explicitly. If we further define a new complex field A such that $M \equiv (f_o^2 N^{-2})\mathcal{A}_z$, then it is also possible to explicitly calculate the leading order pressure by integrating the hydrostatic equation along with the mass conservation equation. In essence, $\mathcal{A}$ incorporates all of the relevant physical quantities of interest. Therefore, we prefer to work solely with the dependent variable $\mathcal{A}$. Substituting the definition of $\mathcal{A}$ into the leading order horizontal velocity solution yields an expression for the demodulated velocity of the NIO

$$u + iv = e^{-f_o t} L\mathcal{A},\tag{2}$$

where

$$L\mathcal{A} \equiv (f_o^2 N^{-2} \mathcal{A}_z)_z.\tag{3}$$

We find that the $\mathcal{O}(\epsilon^2)$ equation contains resonant terms proportional to $e^{-i f_o t}$. To prevent related secular terms from arising in the higher order correction, we require that

$$L\mathcal{A}_t + J(\Psi, L\mathcal{A}) + \frac{i}{2} f_o \nabla^2 \mathcal{A} + \frac{i}{2} \nabla^2 \Psi L\mathcal{A} = 0,\tag{4}$$

where $\nabla^2 = \partial_{xx} + \partial_{yy}$ represents the horizontal Laplacian operator and $J(\Psi, L\mathcal{A}) = \Psi_x(L\mathcal{A})_y - \Psi_y(L\mathcal{A})_x$ is the Jacobian. One advantage of (4) is that the first term on the left hand side has the direct physical interpretation of being the time rate of change of the horizontal velocity. The vertical boundary conditions demand zero vertical velocity at the top and bottom of the ocean, translating into

$$\mathcal{A}_z(x, y, 0, t) = \mathcal{A}_z(x, y, -H, t) = 0\tag{5}$$

where H is the depth of the ocean. This condition follows the rigid lid approximation that assumes the typical amplitude of surface waves are negligible compared to the vertical wavelength of the propagating NIOs. Normalized horizontal boundary conditions are 2π periodic. The initial condition depends on how one chooses to model the passage of the storm or other instigating event. We will specify this condition later. The present study will focus on investigating some of the fundamental characteristics of the NIO equation (4) in the specific context of a simple random wave model of the background turbulent geostrophic eddy field.

3

4   Vertical Normal Modes

The top and bottom boundaries of the ocean have the effect of confining wave energy to a region of finite vertical extent. Thus, the ocean can be considered as a waveguide causing energy to propagate along the horizontal direction. With this notion, we proceed in assuming a solution to (4) in terms of a superposition of vertical normal modes

$$\mathcal{A} = \sum_{m=1}^{\infty} A_m(x,y,t) P_m(z) \sigma_m, \tag{6}$$

where m denotes the vertical wavenumber, $P_m(z)$ represents the eigenfunctions, and σ_m represents the projection of the initial condition onto the vertical normal modes. Note, the expansion in (6) relies on the assumption that the background geostrophic flow is barotropic, i.e. $\Psi_z = 0$. Applying the differential operator L to (6) gives

$$L\mathcal{A} = L(A_m P_m) = (A_m) L P_m. \tag{7}$$

Substituting (7) into (4),

$$\frac{LP_m}{P_m} = \frac{-i(f_o/2)\nabla^2 A_m}{A_{m_t} + J(\Psi, A_m) + i/2(\nabla^2\Psi)A_m} = -R_m^{-2}. \tag{8}$$

For historical reasons [6], eigenvalues are represented as R_m^{-2}, where R_m (dimensions of length) symbolizes the Rossby deformation radius. From (8), we obtain a partial differential equation for A_m

$$A_{m_t} + J(\Psi, A_m) + \frac{i}{2}(\nabla^2\Psi)A_m = \frac{i\hbar_m}{2}\nabla^2 A_m, \tag{9}$$

where $\hbar_m = f_o R_m^2$ will be referred to as the dispersivity[†] associated with the mth vertical mode. Since the initial condition of A has been projected onto vertical normal modes, the initial condition associated with each A_m is simply $A_m(x,y,0) = 1$. Exact numerical values of $\hbar_m$ depend on the eigenvalues of (8) which, in turn, depend on the shape of the buoyancy frequency profile, $N = N(z)$. If we assume N=constant, then $P_m(z) \propto \cos(N^2(f_o R_m)^{-2}z)$ and $R_m = N/f_o\sqrt{H/(m\pi)}$. A constant buoyancy frequency profile, however, is not a reasonable physical model; and therefore, we chose something slightly more realistic. In this regard, we follow the work of Gill [6]. Figure 1 shows the model N profile used here. The corresponding eigenvalues are computed numerically and plotted in figure 2 using a value of $f_o = 1{\times}10^{-4}\text{s}^{-1}$. Of interest is the relatively large range of $\hbar$ values (over four orders of magnitude) apparent just within the first 10 vertical modes. We expect this to play an important role in the developing structure of A. Also, note that for the N profile in figure 1, $\hbar \to m^{-2}$ as compared to $\hbar \to m^{-1/2}$ for the case of N=constant.

[†]This is appropriate nomenclature since (9) begets a dispersion relation. Consider only the time derivative and Laplacian terms; assuming a solution of the form $e^{kx+\ell y-\omega t}$ yields the real-valued dispersion relation $\omega = \hbar(k^2 + \ell^2)$. This is particularly interesting since (9) "looks like" an advection-diffusion equation but because of the i multiplying the Laplacian term, a real-valued dispersion relation is obtained analogous to a wave equation.
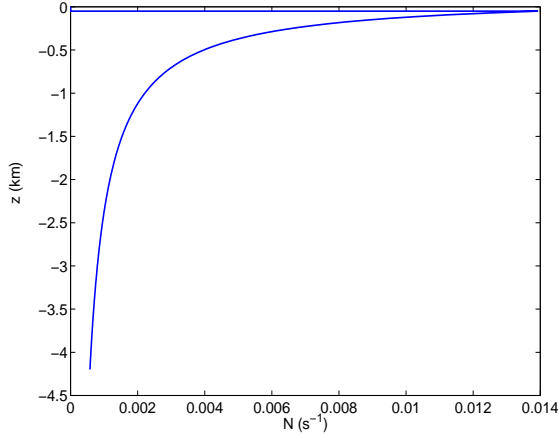
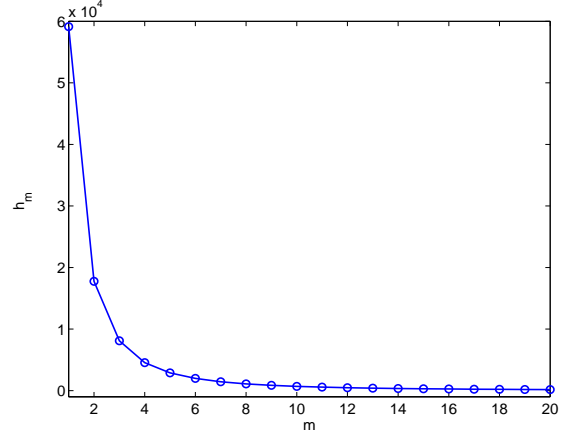Figure 1: Buoyancy frequency profile used to calculate h_m.

Figure 2: Dispersivity as a function of vertical wavenumber m.

Except for the dependence of the dispersivity $\hbar$ on the vertical wavenumber m, A apparently satisfies the same initial value problem regardless of the specific vertical normal mode under consideration. Therefore, in the remainder of the paper, we drop the subscript m on A. Focus is placed on understanding the general behavior of the initial value problem given by

$$A_t + J(\Psi, A) + \frac{i}{2}(\nabla^2\Psi)A = \frac{i\hbar}{2}\nabla^2 A, \qquad A(x, y, 0) = 1 \tag{10}$$

for a range of parameter values $0 \leq \hbar < \infty$ and a specific form of Ψ detailed in section 6. Equation (10) will be referred to as the passive scalar dispersion equation.

5 Scalar Dispersion Equation

An important aspect of (10) is that the quantity $|A|^2$ is conserved over the spatial domain. To see this, we start by writing A in terms of a magnitude R and phase θ

$$A = R\,e^{i\theta}. \tag{11}$$

Substituting (11) into (10), separating real and imaginary parts and dividing by $e^{i\theta_n}$ yields evolution equations for R and θ, respectively,

$$R_t + J(\Psi, R) = \frac{-\hbar}{2}\left[2\nabla R\nabla\theta + R\nabla^2\theta\right], \tag{12}$$

$$\theta_t + J(\Psi, \theta) = \frac{-\zeta}{2} + \frac{\hbar}{2}\left[\frac{\nabla^2 R}{R} - (\nabla\theta)^2\right], \tag{13}$$

where $\zeta = \nabla^2\Psi$ represents the vorticity. Multiplying (12) by R and integrating over the two dimensional spatial domain gives

$$\frac{D}{Dt}\int_{\mathcal{S}}\frac{R^2}{2}\,dS = -\hbar\int_{\mathcal{S}}\nabla(\frac{R^2}{2}\nabla\theta)\,dS = -\hbar\int_{\mathcal{C}}\frac{R^2}{2}\nabla\theta\cdot\hat{r}\,dC = -\hbar\int_{\mathcal{C}}\frac{R^2}{2}\frac{\partial\theta}{\partial r}\,dC, \qquad (14)$$

where $DR/Dt \equiv \partial R/\partial t + J(\Psi, R)$ and $\hat{r}$ is the outward normal unit vector at the boundary. In obtaining (14), we have used the product rule $\nabla R^2/2\nabla\theta = \nabla(R^2/2\nabla\theta) - R^2/2\nabla^2\theta$ and the divergence theorem. Far-field boundary conditions are utilized, which translates into $\nabla A \cdot \hat{r} = 0$, on the boundary; or in polar representation, $\frac{\partial R}{\partial r} = 0$ and $\frac{R^2}{2}\frac{\partial\theta}{\partial r} = 0$, on the boundary. Note, periodic boundary conditions in a two dimensional box automatically satisfy the far-field conditions due to the fact that the gradient of the function at one end of the periodic domain is exactly equal and opposite to the gradient at the other end. Application of the far-field boundary condition to the last expression of (14) leaves

$$\frac{D}{Dt}\int_{V}|A|^2 dV = 0, \qquad (15)$$

which proves our initial statement at the beginning of the section.

We contrast (15) with the case of passive scalar diffusion. The equation governing the evolution of a scalar concentration field c in a background flow can be written as

$$c_t + J(\Psi, c) = \nu\nabla^2 c, \qquad c(x, y, 0) = c_o, \qquad (16)$$

where ν is the molecular diffusivity coefficient, in analogy to the dispersivity of the scalar dispersion equation (10). Following the same procedure for A, we find

$$\frac{D}{Dt}\int_{V}\frac{c^2}{2}dV = -\nu\int_{V}(\nabla c)^2 dV, \qquad (17)$$

We conclude that the diffusion process tends to minimize the squared scalar concentration whereas the dispersion process conserves this same quantity. What does this say about the generation of small scales or the cascade of energy from large to small scales? Does A exhibit a Batchelor scale/spectrum [7]? These questions have motivated, to some extent, the work herein. At this point, we present the specific streamfunction model used for the remainder of the calculations in the paper.

6 Two Stage Random Wave Model

We will investigate the behavior of (10) for the specific two dimensional, random flow field described by the following streamfunction Ψ

$$\Psi_n = \begin{cases} \sin(y + \phi_n), & 2n\tau < t \le (2n+1)\tau, \\ \cos(x + \chi_n), & (2n+1)\tau < t \le (2n+2)\tau, \end{cases} \qquad (18)$$

for $n = 0, 1, \ldots$, where ϕ, χ are uniform random phases between 0 and 2π and τ represents a characteristic decorrelation time of the turbulence. A variation of this model has been used in the past, [8]. Note, we have nondimensionalized Ψ by a characteristic streamfunction Ψ_o and

the spatial coordinates by a characteristic horizontal wavenumber κ_h. The spatial domain is thus 2π periodic. In order for the model to have physical relevance to the oceanic geostrophic eddy field, we have taken $\Psi_o = 3000\text{m}^2/\text{s}$ and $\kappa_h = 6 \times 10^{-5} \text{m}^{-1}$, based on the data of [1]. Together, these give a characteristic decorrelation time scale of $\tau^* = \mathcal{O}(1\text{day})$. The velocity components, $\vec{u} = (u, v)$, follow from the definition of the streamfunction as $u = -\Psi_y$ and $v = \Psi_x$. The corresponding particles trajectories are

$$x_{n+1} = x_n - \cos(y_n + \phi_n)t, \qquad {\scriptstyle 2n\tau < t \leq (2n+1)\tau} \tag{19}$$

$$y_{n+1} = y_n + \cos(x_{n+1} + \chi_n)t \qquad {\scriptstyle (2n+1)\tau < t \leq (2n+1)\tau.} \tag{20}$$

As apparent, the flow model is characterized by a two stage advection process. In the first stage, during time intervals $2n\tau < t \leq (2n+1)\tau$, particles are advected in the x direction only for a time τ; while in the second stage, during $(2n + 1)\tau < t \leq (2n + 1)\tau$, particles are advected in the y direction only for a time τ. The combination of these two advection stages constitutes a single step in the random wave model. The total time to complete n steps is then $t = n(2\tau)$. The main advantage of the two stage random model stems from simplifications in the subsequent mathematics as will be described later. It is worthwhile to analyze the two stage random flow field in terms of the effect on material line stretching and fluid particle diffusivity. We compare the two stage model of (18) with a one stage model such as the rennovating random wave model,

$$\Psi_n = \cos\left[x \cos\phi_n + y \sin\phi_n + \chi_n\right], \quad (n-1)\tau < t \leq n\tau, \tag{21}$$

where advection is performed in a single stage.

6.1 Material line stretching

We investigate material line stretching induced by (19–20) in the context of Lyapunov exponents. Lyapunov exponents are used extensively in the study of nonlinear dynamical systems as a measure of whether two initial conditions diverge exponentially in time, thus possibly leading to the onset of chaos. The same concept is often applied to neighboring fluid particles in the study of fluid turbulence. In this manner, the Lyapunov exponent gives some indication of the stretching of differential line elements in the flow. In the case of advection of a real-valued passive scalar, this can be directly related to the development of spatial gradients in the scalar field. We will consider later whether an analogy to the complex-valued scalar A exists.

6.1.1 Lyapunov exponent: background

We follow the general definitions and methodology of Seydel [9] regarding the Lyapunov exponent calculations. An initially small ring of fluid particles with initial radius ρ_o deforms into an ellipse with major axis μ due to regions of localized strain in the flow. Linearizing the flow about the origin $\rho_o = 0$, we obtain $\vec{h}_n = \mathbf{J}^n \vec{h}_o$ where $\mathbf{J}$ denotes the Jacobian matrix of the random map given by (19–20), and $\vec{h}_o$, $\vec{h}_n$ describe the particle positions in the original (circular) and deformed (elliptic) configurations, respectively. Strictly, $\vec{h}_n$ and $\vec{h}_o$ must be

differential vectors for the linearization to be valid. We look for exponential stretching of the form $\|\vec{h}_n\|^2 = (\|\vec{h}_o\|\,e^{Lt})^2$ where L denotes the Lyapunov exponent. Rearranging and taking the limit as $t \to \infty$ leads to

$$L = \lim_{n \to \infty} \frac{1}{4n\tau} \ln\left(\frac{\|\mathbf{J}^n \vec{h}_o\|}{\|\vec{h}_o\|^2}\right), \tag{22}$$

where we have substituted in $t = 2n\tau$ with 2τ denoting the decorrelation time associated with the two stage random wave model of (19–20). Since $\mathbf{J}$ describes a random process, we ensemble average (denoted as $\langle \cdot \rangle$) over the random variables ϕ_n and χ_n so that L does not depend on a particular realization. Additionally, we use the identity $\|\mathbf{J}^n \vec{h}_o\|^2 = \vec{h}_o^{\mathrm{T}}(\mathbf{J}^{n^{\mathrm{T}}}\mathbf{J}^n)\vec{h}_o$ to simplify (22). The resultant definition of the Lyapunov exponent used herein is

$$L = \lim_{n \to \infty} \frac{1}{4n\tau} \ln\left(\frac{\vec{h}_o^{\mathrm{T}} \langle \mathbf{K} \rangle \, \vec{h}_o}{\vec{h}_o^{\mathrm{T}} \vec{h}_o}\right), \tag{23}$$

where $\mathbf{K} = \mathbf{J}^{n^{\mathrm{T}}}\mathbf{J}^n$. Note, for convenience, we have taken $\langle \mathbf{K} \rangle$ rather than $\langle \ln \mathbf{K} \rangle$. The ramifications of this subtle difference stem from the fundamental differences between additive and multiplicative random walks as detailed by Redner [10]; but it is not a primary concern of the present study.

6.1.2 Lyapunov exponent: two stage random wave model

We now want to explicitly calculate the Lyapunov exponent defined in (23) for the two stage random wave model given by (19–20). During the nth step of the random walk, $\mathbf{J}_n = \mathbf{J}_{\mathrm{II}}(\chi_n)\mathbf{J}_{\mathrm{I}}(\phi_n)$, where $\mathbf{J}_{\mathrm{I}}$ and $\mathbf{J}_{\mathrm{II}}$ describe advection in the x direction (first stage) and y direction (second stage), respectively. From (19–20),

$$\mathbf{J}_{\mathrm{I}}(\phi_n) = \begin{bmatrix} 1 & \sin(y_n + \phi_n)\tau \\ 0 & 1 \end{bmatrix}, \quad \text{and} \quad \mathbf{J}_{\mathrm{II}}(\chi_n) = \begin{bmatrix} 1 & 0 \\ -\sin(x_{n+1} + \chi_n)\tau & 1 \end{bmatrix}. \tag{24}$$

The independence of each step allows the ensemble average of $\mathbf{K}$ after n steps to be written as

$$\langle \mathbf{K} \rangle = \langle \mathbf{J}_{\mathrm{I}}^{\mathrm{T}}(\phi_1)\langle \mathbf{J}_{\mathrm{II}}^{\mathrm{T}}(\chi_1) \ldots \langle \mathbf{J}_{\mathrm{I}}^{\mathrm{T}}(\phi_n)\langle \mathbf{J}_{\mathrm{II}}^{\mathrm{T}}(\chi_n)\mathbf{J}_{\mathrm{II}}(\chi_n)\rangle \mathbf{J}_{\mathrm{I}}(\phi_n)\rangle \ldots \mathbf{J}_{\mathrm{II}}(\chi_1)\rangle \mathbf{J}_{\mathrm{I}}(\phi_1)\rangle. \tag{25}$$

Introducing the diagonal matrix $\mathbf{\Gamma} = \begin{bmatrix} a & 0 \\ 0 & b \end{bmatrix}$, the inner most ensemble average of $\langle \mathbf{K} \rangle$ can be written as $\langle \mathbf{J}_{\mathrm{II}}^{\mathrm{T}}(\chi_n)\,\mathbf{\Gamma}\,\mathbf{J}_{\mathrm{II}}(\chi_n)\rangle$. Upon calculating several sequential ensemble averages, the recurrsion relation for $\vec{a} = (a, b)$ becomes apparent. After n steps, we find

$$\begin{bmatrix} a_{n+1} \\ b_{n+1} \end{bmatrix} = \begin{bmatrix} 1 & \frac{\tau^2}{2} \\ \frac{\tau^2}{2} & 1 + \frac{\tau^4}{4} \end{bmatrix} \begin{bmatrix} a_n \\ b_n \end{bmatrix}, \tag{26}$$

where $a_0 = b_0 = 1$. With this, the general form of the Lyapunov exponent (23) reduces to

$$L = \lim_{n \to \infty} \frac{1}{4n\tau} \ln\left([h_1\, h_2] \begin{bmatrix} a_n & 0 \\ 0 & b_n \end{bmatrix} \begin{bmatrix} h_1 \\ h_2 \end{bmatrix}\right). \tag{27}$$
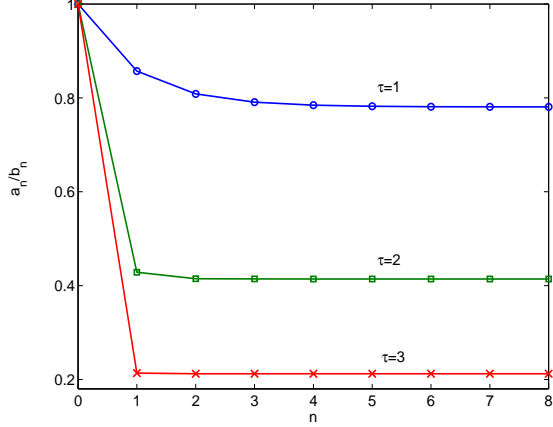
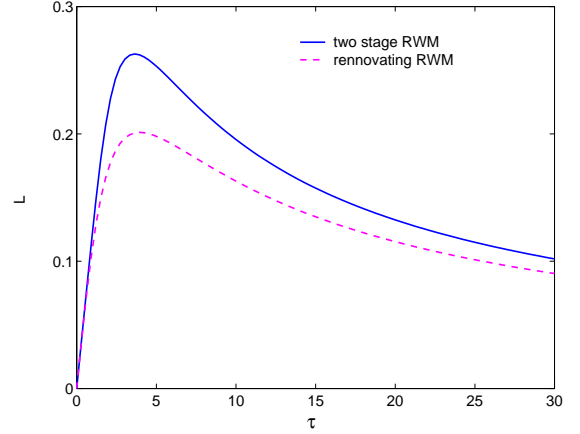Figure 3: Ratio of the two diagonal terms in the stretching matrix as a function of steps n in the random map.

Figure 4: Lyanpunov exponent L as a function of turbulent decorrelation time τ.

In order to represent $\vec{a}_n$ in terms of $\vec{a}_0$ we need to solve the corresponding eigenproblem, $\mathbf{M}\vec{v} = \lambda\vec{v}$, with $\mathbf{M}$ as given in (26). Due to space limitations, we do not provide the details of this calculation. The main result is $\vec{a}_n = \mathbf{R}\mathbf{\Lambda}_n\mathbf{R}^{\mathrm{T}}\vec{a}_0$, where $\mathbf{R}$ is the rotation matrix, $\mathbf{R} = \begin{bmatrix} v_1^+ & v_1^- \\ v_2^+ & v_2^- \end{bmatrix}$, and $\mathbf{\Lambda}_n = \begin{bmatrix} \lambda^{+n} & 0 \\ 0 & \lambda^{-n} \end{bmatrix}$. After performing the algebra, we find

$$a_n = \frac{2^{-1-3n}}{16 + \tau^4}\left[(16 + \tau^4 + (\tau^2 - 4)\sqrt{16 + \tau^4})(8 + \tau^4 - \tau^2\sqrt{16 + \tau^4})^n + \right.$$
$$\left. (16 + \tau^4 - (\tau^2 - 4)\sqrt{16 + \tau^4})(8 + \tau^4 + \tau^2\sqrt{16 + \tau^4})^n\right], \quad (28)$$

$$b_n = 2^{-1-3n}\left[\frac{(4 + \tau^2 + \sqrt{16 + \tau^4})(8 + \tau^4 + \tau^2\sqrt{16 + \tau^4})^n}{\sqrt{16 + \tau^4}} - \right.$$
$$\left. \frac{(\tau^2 - 4 + \sqrt{16 + \tau^4})(8 + \tau^4 - \tau^2\sqrt{16 + \tau^4})^n}{16 + \tau^4 + \tau^2\sqrt{16 + \tau^4}}\right]. \quad (29)$$

Notice, a_n and b_n are not equal; therefore, stretching is anisotropic in this flow field. In fact, looking at the simple case of $n = 1$, $a_1 = 1 + \tau^2/2$ and $b_1 = 1 + \tau^2/2 + \tau^4/4$; we see that more stretching occurs in the y direction as compared to the x direction. However, at long times, taking the limit as $n \to \infty$, we find that the stretching does become isotropic as shown in the following. We rewrite (27) as

$$L = \lim_{n\to\infty}\frac{1}{4n\tau}\ln\left(h_1^2\frac{a_n}{b_n} + h_2^2\right) + \lim_{n\to\infty}\frac{1}{4n\tau}\ln(b_n). \quad (30)$$

As $n \to \infty$, $\frac{a_n}{b_n} = -\frac{\tau^2}{4} + \frac{\sqrt{16 + \tau^4}}{4}$. Figure 3 shows a_n/b_n as a function of n for a family of three τ values. We see that for any given τ, a_n/b_n asymptotes to a constant value. Therefore,

9

in the limit as $n \to \infty$, the first term in (30) goes to zero. At large n, b_n remains as the only contribution to L and thus stretching becomes isotropic. From figure 3, one can determine how quickly the flow becomes isotropic for a given τ. We see that for $\tau = 3$, stretching becomes isotropic after the first step.

With further manipulation of (27) we obtain the functional relation between L and τ

$$L = \frac{1}{4\tau} \ln \left[(1 + \tau^4/8) + \frac{\tau^2}{8} \sqrt{\tau^4 + 16} \right]. \tag{31}$$

Figure 4 shows the graphical representation of (31) compared with that obtained for the rennovating random wave model of (21). Maximum stretching in the two stage random wave model occurs at $\tau = 3.64$ in contrast to $\tau = 3.94$ for the one stage random model. In general, the two stage random wave model generates more stretching of the fluid elements.

6.2 Diffusivity of fluid particles

We follow Einstein's theory of Brownian movement [11] to determine the diffusivity associated with the movement of fluid particles in the random wave model of (19–20). For a random walk processes in two dimensions, Einstein showed that

$$\overline{\Delta^2}_n = 4D_{\text{eff}}t, \tag{32}$$

where Δ is the particle displacement, an overline denotes an average performed over n steps in the random walk, and D_{eff} is the effective diffusion coefficient that appears in the scalar diffusion equation. Since each of the steps in the random walk is independent, $\overline{\Delta^2}_n = n\Delta^2 = \Delta^2 t/\tau$, where t is the total time and τ represents the decorrelation time of the random walk. In our particular case, particle displacements during the nth step can be written as $r_n^2 = r_{I_n}^2 + r_{II_n}^2$, where r_I, r_{II} are the displacements during the x, y stages of advection, respectively. Without loss of generality, we can make the coordinate translation $(x_n, y_n) \to (0,0)$ before each nth step. Applying this simplification to (19–20) gives

$$r_n^2 = \tau^2 \cos^2(\phi_n) + \tau^2 \cos^2(-\cos(\phi_n)\tau + \chi_n). \tag{33}$$

Because we want the calculation to be independent of the random phase angles associated with a particular realization, we ensemble average over both ϕ and χ to yield $\langle r^2 \rangle_{\phi,\chi} = \tau^2$. Note, in analogy to (32), $\Delta^2 = \langle r^2 \rangle_{\phi,\chi}$. Taking the average of $\langle r^2 \rangle_{\phi,\chi}$ over n total steps in the random walk and using (32) gives the resultant particle displacement diffusivity of $D_{\text{eff}} = \frac{\tau}{8}$. It is interesting to note that this diffusivity is identical to that of the rennovating random wave model (21) where advection is performed in a single step. At this point, there is some confidence in our understanding of the model flow field; we, therefore, proceed to study the behavior of the scalar dispersion equation (10) under the two limiting parameter conditions of $\hbar = 0$ and $\hbar \to \infty$.

7 Zero Dispersion Limit

In the case $\hbar = 0$, the scalar dispersion equation (10) along with (18) reduces to

$$A_t - \cos(y + \phi)A_x - \frac{i}{2}\sin(y_+\phi)A = 0, \quad {\scriptstyle 2n\tau < t \leq (2n+1)\tau,} \tag{34}$$

$$A_t - \cos(x + \chi)A_y - \frac{i}{2}\sin(x + \chi)A = 0, \quad {\scriptstyle (2n+1)\tau < t \leq (2n+2)\tau.} \tag{35}$$

We solve the above set of equations using the method of characteristics. In the first stage of the random wave model, we define new variables $\tilde{x} = x + c_\mathrm{I}t$, $\tilde{t} = t$, $\tilde{y} = y$; while in the second stage, we define $\tilde{y} = y + c_\mathrm{II}t$, $\tilde{t} = t$, $\tilde{x} = x$ where $c_\mathrm{I} = \cos(y + \phi)$ and $c_\mathrm{II} = \cos(x + \chi)$. This effectively removes the advective terms from (34) simplifying the problem to two, uncoupled, first order ordinary differential equations, one at each advection stage. The solutions valid in the first and second stages are

$$A_\mathrm{I} = A_o e^{i/2 \sin(\tilde{y}+\phi)\tilde{t}} \quad \text{and} \quad A = A_\mathrm{I} e^{i/2 \sin(\tilde{x}+\chi)\tilde{t}}, \tag{36}$$

respectively, where A_o represents the initial condition at the beginning of the nth step. Recall, at $n = 0$, $A(x, y, t=0) = 1$. Using the fact that $\tilde{x}$ and $\tilde{y}$ remain constant along characteristic curves, the solution can be written in terms of an iterated map

$$\scriptstyle 2n\tau < t \leq (2n+1)\tau : \displaystyle A_{\mathrm{I}\,n+1} = A_n\, e^{i/2 \sin(y_n + \phi_n)\tau}, \qquad x_{n+1} = x_n - \cos(y_n + \phi_n)\tau, \tag{37}$$

$$\scriptstyle (2n+1)\tau < t \leq (2n+1)\tau : \displaystyle A_{n+1} = A_{\mathrm{I}\,n+1}\, e^{i/2 \sin(x_{n+1} + \chi_n)\tau}, \qquad y_{n+1} = y_n + \cos(x_{n+1} + \chi_n)\tau. \tag{38}$$

Figure 5 displays four snapshots of $\Re(A)$ as computed from the map above for the case of $\tau = 1$. The resolution is 1028×1028. Later, we will compare these pictures to the structure of $\Re(A)$ for $\hbar \neq 0$. From (37) and (38), it is apparent that no mechanism exists to instigate changes in $|A|$; therefore, $|A|$ remains constant at its initial value of unity. This agrees with the previous results of section 5. However, the phase of A, denoted by θ as in (11), does exhibit interesting behavior. The iterated map for θ follows directly from (37–38) as

$$\theta_{n+1} = \theta_n + \sin(y_n + \phi_n)\frac{\tau}{2} + \sin(x_{n+1} + \chi_n)\frac{\tau}{2}, \tag{39}$$

where x_{n+1} and y_{n+1} are given as in (37) and (38). We observe that for $\hbar = 0$, θ undergoes a random walk process and therefore has an associated diffusivity D_θ (not to be confused with the diffusivity of particle trajectories). To calculate D_θ, we follow the procedure in section 6.2. The ensemble averaged variance of θ is defined as $\langle \theta'^2 \rangle_{\phi,\chi} = \langle (\theta_{n+1} - \theta_n)^2 \rangle$. Substituting in (39) and performing the average yields $\langle \theta'^2 \rangle = \tau^2/4$. Making the analogy with Einstein's theory in (32), we have $\Delta^2 = \langle \theta'^2 \rangle_{\phi,\chi}$. Taking the average of Δ^2 over n total steps in the random walk and using (32)[†] gives the resultant phase diffusivity $D_\theta = \tau/16$.

This is an interesting result in that the behavior of θ for zero dispersivity undergoes a normal diffusion process analogous to that of a real passive scalar. The structure of θ after 25 iterations of the map in (39), for $\tau = 1$, is shown in figure 6. Note, in order to obtain a continous field, results are plotted as $\theta/2\pi$. The initial condition at $t = 0$ is $\theta = 0$ and the resolution is 1028×1028. This picture looks surprisingly similiar to the stirring of a passive scalar as presented in [8] (figure 1 of that paper), for a random velocity field nearly equivalent to that of (18).

[†]In the case of θ, we have a one dimensional random walk given by $\overline{\Delta^2}_n = 2D_\mathrm{eff}t$.
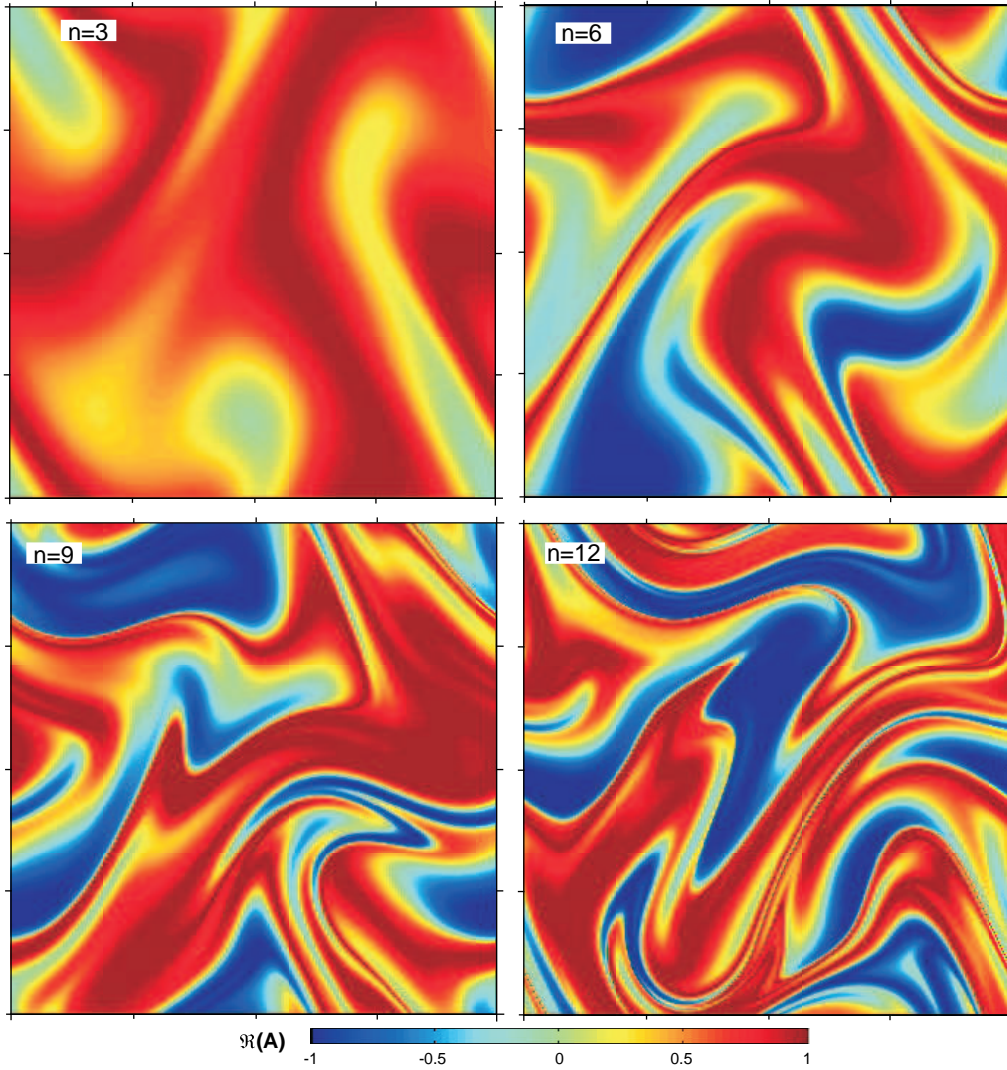
Figure 5: Snapshots of the spatial structure of $\Re(A)$ for the $\tau = 1$, $\hbar = 0$. Recall that at $n = 0$, $\Re(A) = 1$.

8 Strong Dispersion Limit

We use a simple multiscale analysis to investigate the large $\hbar$ behavior of (10) by introducing a small parameter ϵ and a slow time t' such that $\hbar = \mathcal{O}(1/\epsilon)$ and $t' = \epsilon t$. Applying these scalings to (10) and multiplying by ϵ gives

$$A_{t'} + \epsilon J(\Psi, A) + \epsilon \frac{i\zeta}{2} A = \frac{i}{2} \nabla^2 A. \tag{40}$$

We assume that the solution can be written as a power series expansion in ϵ, $A = A_0 + \epsilon A_1 + \epsilon^2 A_2 + \dots$. The $\mathcal{O}(1)$ equation is obtained by substituting this expansion into (40) and taking the limit as $\epsilon \to 0$
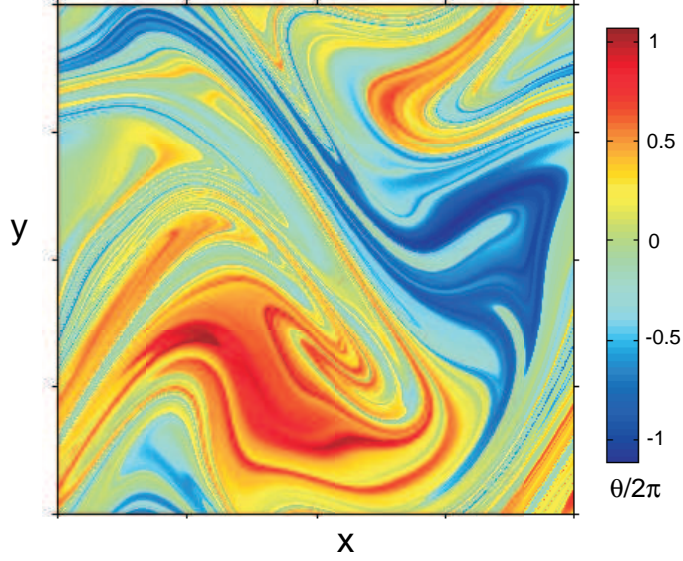
Figure 6: Phase of A for the case of $\hbar = 0$, $\tau = 1$ after 25 random advection steps.

$$\mathcal{O}(1): \quad A_{0_{t'}} = \frac{i}{2}\nabla^2 A_0 \tag{41}$$

with the initial condition $A_0(t=0)=1$. The solution $A_0 = 1$ trivially satisfies this initial value problem. The $\mathcal{O}(\epsilon)$ equation is obtained by substituting the $\mathcal{O}(1)$ solution into (40), dividing by ϵ, and taking the limit as $\epsilon \to 0$

$$\mathcal{O}(\epsilon): \quad A_{1_{t'}} + \frac{i\zeta}{2} = \frac{i}{2}\nabla^2 A_1 \tag{42}$$

with the initial condition $A_1(t=0)=0$. Note, $J(\Psi, A_0) = 0$. Because of the explicit form of ζ, see (18), we need to consider the two stages of the advection process separately. This complicates the problem in that the initial condition for each advection stage depends on the final state at the end of the previous advection stage. We start by considering the first time interval $0 < t \leq \tau$, during which $\zeta = -\sin(y + \phi)$ and (42) reduces to

$$A_{1_{t'}} - \frac{i}{2}\nabla^2 A_1 = -\frac{i}{2}\sin(y + \phi). \tag{43}$$

with $A_1(t=0)=0$. We require both the homogeneous and particular parts of the solution to vanish at $t=0$. Therefore, the homogenous part of the solution is simply 0. We assume a particular solution of the form $A_1 = \tilde{a}(t')\sin(y + \phi)$. Substituting this into (43), we obtain an ordinary differential equation for $\tilde{a}(t')$, the solution of which is $\tilde{a}(t') = 1 - e^{-it'/2}$. Thus, in the first time interval,

$$A = 1 + \frac{1}{\hbar}(1 - e^{-\frac{it}{2\hbar}})\sin(y + \phi) + \mathcal{O}(\epsilon^2), \quad 0 < t \leq \tau. \tag{44}$$

13

In the subsequent time interval $\tau < t \leq 2\tau$, $\zeta = -\sin(x + \chi)$ and the initial condition is $A_1(t=\tau) = (1 - e^{-\frac{i\tau}{2\hbar}})\sin(y + \phi)$. Following the same procedure used above, we find

$$A = 1 + \frac{1}{\hbar}\left[1 + e^{-\frac{i}{2\hbar}(t-\tau)}\left((1 - e^{-\frac{i\tau}{2\hbar}})\sin(y + \phi) + 1\right)\right]\sin(x+\chi) + \mathcal{O}(\epsilon^2), \quad \tau < t \leq 2\tau. \quad (45)$$

One thing to notice in the strong dispersion limit is that spatial structure in A develops very slowly, in stark contrast to the case of $\hbar = 0$ where, after only 12 iterations, the structure of A has become highly stretched and contorted (see figure 5). We will return to these results later in section 10 to ascertain how the energy contained in the large scales of A varies as a function of $\hbar$. We now consider the regime $\hbar \neq 0$.

9   Numerical Solution for $\hbar \neq 0$

Both the spatial domain and the streamfunction are 2π periodic; therefore, we seek a general solution to (10) in the form of a Fourier series expansion

$$A = \sum_{k,\ell=-\infty}^{\infty} a_{k,\ell}(t)\, e^{ik\,x+i\ell\,y}, \quad a_{k,\ell}(0) = \begin{cases} 1, & \text{if } k = \ell = 0, \\ 0, & \text{otherwise} \end{cases} \quad (46)$$

where $\vec{\kappa} = (k, \ell)$ describes the wavenumber vector and $a_{k,\ell}(t)$ are the corresponding Fourier coefficients. Substituting (46) into (10) yields

$$\sum_{k,\ell=-\infty}^{\infty}\left[\dot{a}_{k,\ell} + i\ell\,\Psi_x\,a_{k,\ell} - ik\,\Psi_y\,a_{k,\ell} + \frac{i}{2}\nabla^2\Psi a_{k,\ell}\right] e^{\vec{\kappa}\cdot\vec{x}} = -\frac{i\hbar}{2}\sum_{k,\ell=-\infty}^{\infty}(k^2 + \ell^2)a_{k,\ell}\, e^{\vec{\kappa}\cdot\vec{x}}. \quad (47)$$

In order to eliminate the summations, we utilize the fact that the Fourier modes are orthogonal. To exploit this, we multiply (47) by $e^{-iqy-ipx}$ and integrate over $y = 0\text{--}2\pi$ and $x = 0\text{--}2\pi$. Integrations are performed in detail in the Appendix. It is worth noting that if we did not chose a two stage random wave model for the velocity field, but rather used a single stage model such as (21), then it would not be possible to analytically integrate the terms resulting from (47). Performing the integrations yields two sets of coupled, first order ordinary differential equations for $a_{k,\ell}(t)$, each valid in one of the two stages of the advection process

$$\dot{a}_{k,\ell} + a_{k,\ell+1}\,e^{-i\phi}\left(\frac{1 - i2k}{4}\right) - a_{k,\ell-1}\,e^{i\phi}\left(\frac{1 + i2k}{4}\right) = \frac{-i\hbar}{2}(k^2 + \ell^2)a_{k,\ell}, \quad (48)$$

$$\dot{a}_{k,\ell} + a_{k+1,\ell}\,e^{-i\chi}\left(\frac{1 + i2\ell}{4}\right) - a_{k-1,\ell}\,e^{i\chi}\left(\frac{1 - i2\ell}{4}\right) = \frac{-i\hbar}{2}(k^2 + \ell^2)a_{k,\ell}, \quad (49)$$

for $n = 0, 1, \ldots$ and $k, \ell = -\infty, \ldots, -1, 0, 1, \ldots, \infty$ where (48) and (49) are valid during the time intervals $2n\tau < t \leq (2n + 1)\tau$ and $(2n + 1)\tau < t \leq (2n + 2)\tau$, respectively. The apparent coupling between nearest neighbors of a results directly from the fact that the

14

imposed velocity field contains only one Fourier component, the lowest nonzero wavenumber component. A convenient aspect of the two stage random wave velocity field is that, in the first stage, coupling occurs only between ℓ wavenumbers; while, in the second stage, coupling occurs only between k wavenumbers.
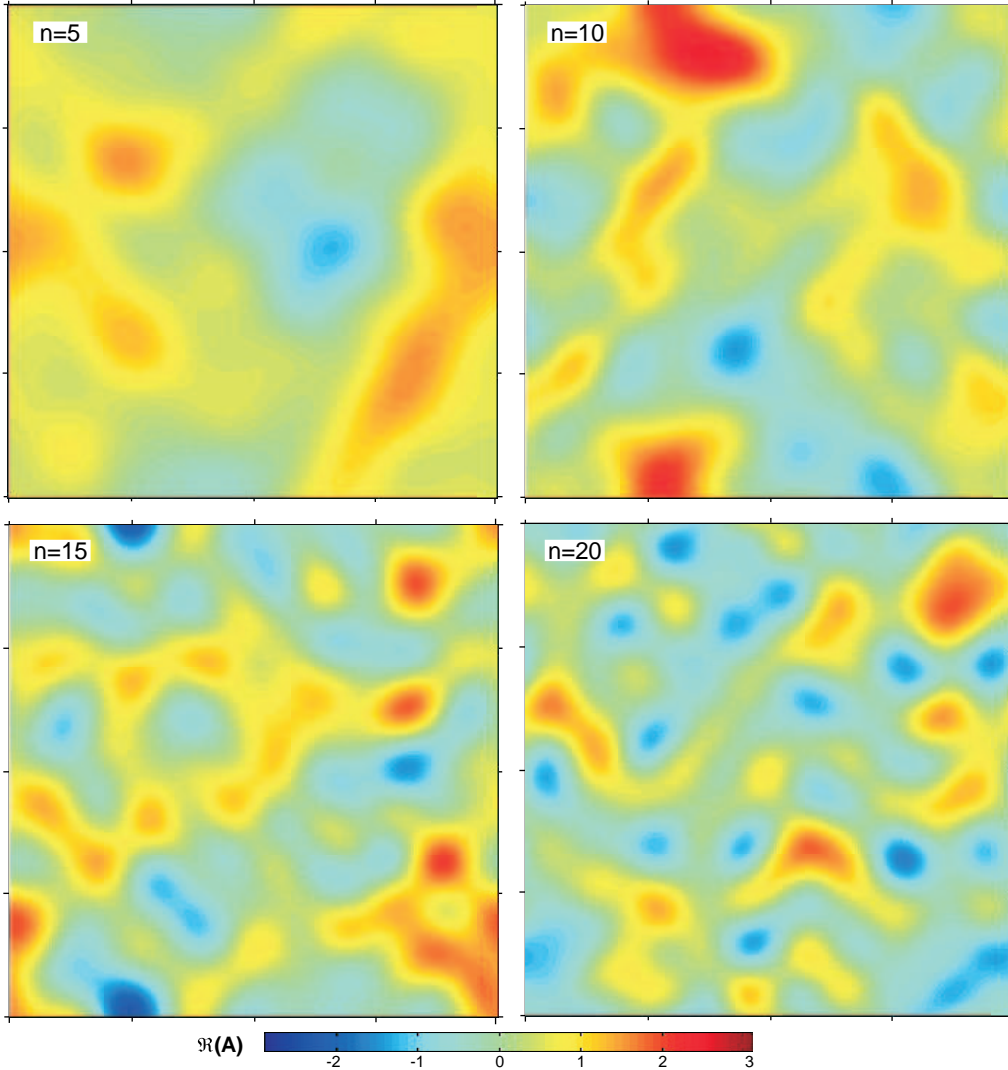

Figure 7: Snapshots of the spatial structure of $\Re(A)$ for the $\tau = 1$, $\hbar = 1$. Recall that at $n = 0$, $\Re(A) = 1$.

We solve (48–49) numerically to obtain the time evolution of the Fourier coefficients $a_{k,\ell}$, then utilize an inverse fast Fourier transform (FFT) algorithm to perform the resummation in (46) to obtain A. In the numerical solution, k, ℓ must be truncated at the Nth Fourier mode, i.e. the summation appearing in (46) occurs over $-N \leq k, \ell \leq N$. We chose N such that the amplitudes of the corresponding Fourier modes at $|k|, |\ell| \geq N$ have decreased below a set tolerance. In practice, though, we typically over resolve the Fourier domain by a substantial

amount since we favor a grid size of $2^p \times 2^p$, $p = 0, 1, 2, \ldots$.

The two truncated systems can each be described by a matrix equation, written in the general, compact form

$$\dot{\vec{y}}(t) = \vec{f}(t, \vec{y}(t)). \tag{50}$$

For example, considering the simple case of $N = 2$, (50) becomes

$$\begin{bmatrix} \dot{a}_{-2} \\ \dot{a}_{-1} \\ \dot{a}_0 \\ \dot{a}_1 \\ \dot{a}_2 \end{bmatrix} = \begin{bmatrix} c & d & 0 & 0 & 0 \\ b & c & d & 0 & 0 \\ 0 & b & c & d & 0 \\ 0 & 0 & b & c & d \\ 0 & 0 & 0 & b & c \end{bmatrix} \begin{bmatrix} a_{-2} \\ a_{-1} \\ a_0 \\ a_1 \\ a_2 \end{bmatrix}, \tag{51}$$

where $b = (1 + i2k)/4\, e^{i\phi_n}$, $c = -i\hbar/2(k^2 + \ell^2)$, $d = -(1 - i2k)/4\, e^{-i\phi_n}$, in the first stage; and $b = (1 - i2\ell)/4\, e^{i\chi_n}$, $c = -i\hbar/2(k^2 + \ell^2)$, $d = -(1 + i2\ell)/4\, e^{-i\chi_n}$, in the second stage. We use the tridiagonal structure of (51) to our advantage in selecting a discretization method. The second order, fully implicit Adams-Moulton method is used in the present study. Applying this discretization method to (50) gives

$$\frac{\vec{y}_{m+1} - \vec{y}_m}{\delta t} = \frac{\vec{f}_{m+1} - \vec{f}_m}{2}. \tag{52}$$

The numerical method conveniently perserves the tridiagonal structure of the original truncated system. At each time step, we solve two, uncoupled linear, tridiagonal systems for $a_{k,\ell}(t)$ (one during each advection stage) with an efficient tridiagonal system solver. A numerical C code was written to compute the time evolution of $a_{k,\ell}$ and perform the subsequent inverse FFT to obtain the spatio-temporal structure of A. Since C does not have built-in capability for handling complex numbers, special functions were written to deal with complex number operations.

There are some additional comments worth mentioning regarding the present numerical scheme. At each time step we verify that the code conserves $|A|^2$ over the spatial domain (refer to section 5) by tracking $a_{0,0}$. The deviation of $a_{0,0}$ from the expected value of unity is never greater than 1×10^{-10}. Additional calculations regarding the stability and accuracy of the present numerical scheme were performed; however, due to space limitations, we do not provide those details. The analyses stem from a comparison between the solution to the discretized equation and the analytical solution obtained in section 8. We found the numerical method to be unconditionally stable. Furthermore, we found that the minimum time step required to achieve a specified accuracy depended on $\hbar$ and the magnitude of the wavenumber κ^2. For example, to achieve 98% accuracy in the highest wavenumber component of the numerical solution for $\hbar = 1$, a minimum time step of 0.005 is required.

Figure 7 displays four snapshots of the spatial structure of $\Re(A)$ for the case of $\hbar = 1$, $\tau = 1$. The resolution in each picture is 1028×1028. Figure 8 displays the numerical results from a comparison study between four different parameter values of $\hbar = 0$, 0.1, 1, and 10. Only the real part of A is shown, although the imaginary part exhibits similar structure. The snapshots are taken at $n = 10$ with $\tau = 1$. All computations utilized the same random data set for ϕ and χ.
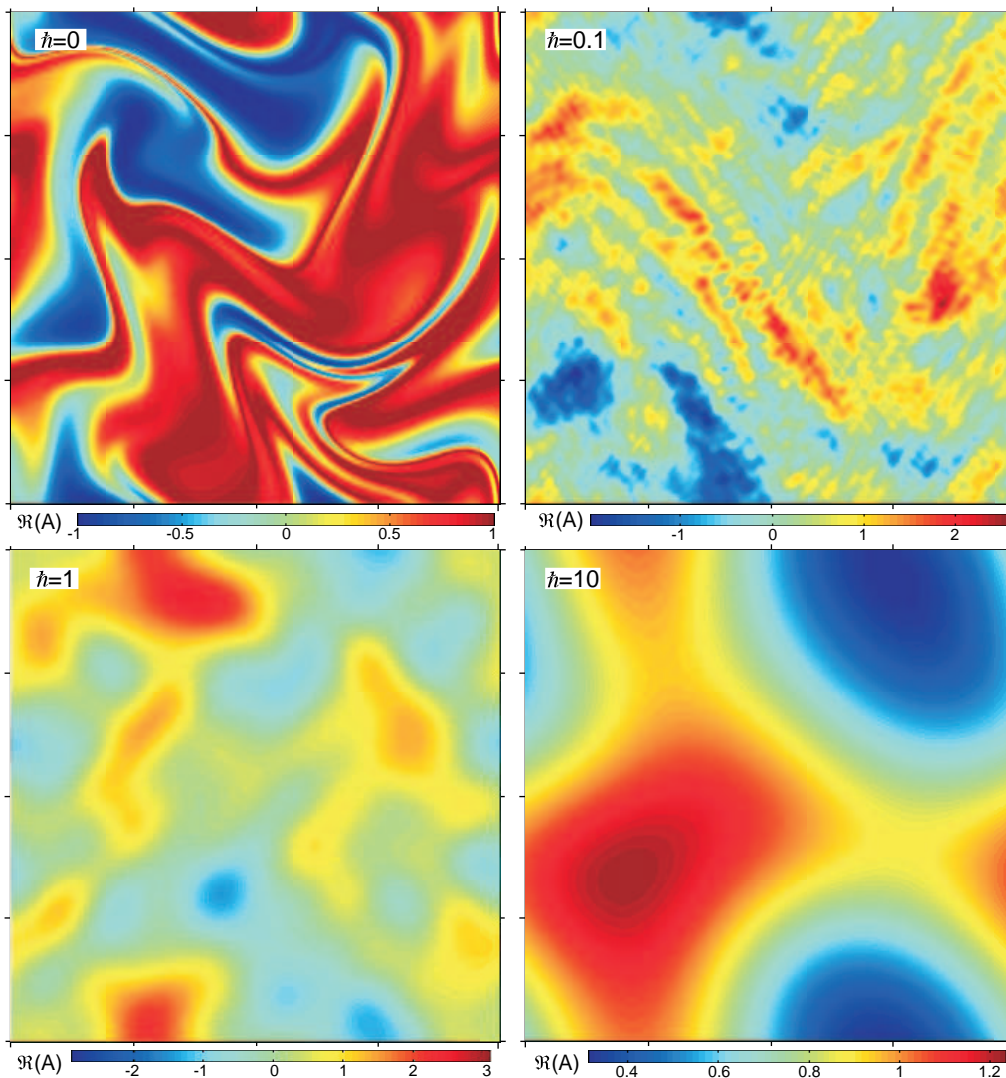
16

Figure 8: Comparison of the spatial structure of $\Re(A)$ for four different $\hbar$ values of 0, 0.1, 1, 10. All snapshots were taken at $n = 10$, $\tau = 1$ and utilize the same random data set for ϕ, χ.

10 Energy in Large Scales

We now take a look at how the energy in the large scales decays in time as a function of $\hbar$. Recall from section 5 that $\langle AA^* \rangle$ represents a conserved quantity where $\langle \cdot \rangle$ denotes a spatial average and the superscript * denotes the complex conjugate. Therefore, we will define the energy associated with the complex scalar A as

$$\varepsilon = \langle A \rangle \langle A^* \rangle. \tag{53}$$

Figure 9 shows the results of ε for three different cases of $\hbar = 0$, 0.01, 1 as computed from the numerical code presented in section 9. The results are for one particular realization only.
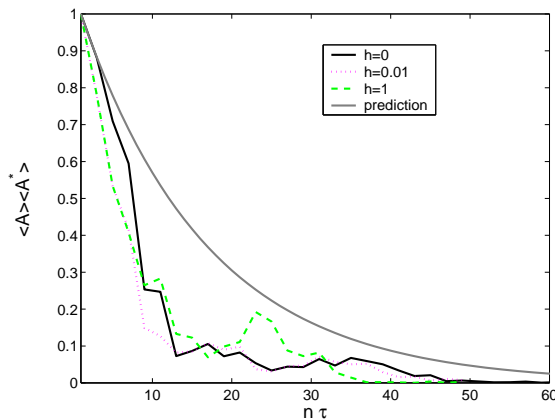
17

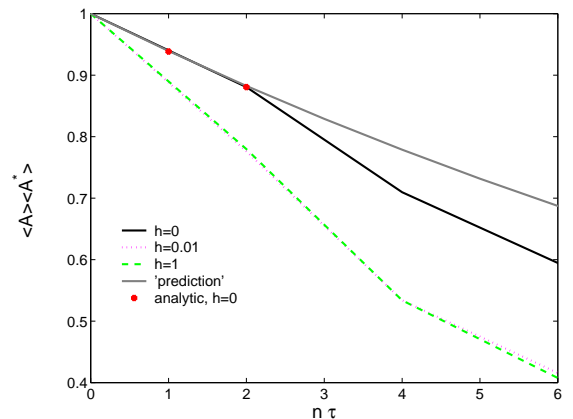Figure 9: Decay of energy in the large scales of A for $\tau = 1$.

Figure 10: Expanded view of figure 9 in the region near $t = 0$.

The exponential prediction shown stems from the hypothesis that the spatial average in the definition of (53) can be replaced by an ensemble average, i.e. $\langle A \rangle = E[\mathrm{e}^{i\theta}]$, where $E[\cdot]$ denotes the expectation of the random process. For the case of $\hbar = 0$, we showed in section 7 that θ obeys a random walk; therefore, the probability of θ is Gaussian. According to the prediction,

$$\langle A \rangle = \int_{-\infty}^{\infty} \frac{\mathrm{e}^{-\theta^2/2\sigma^2}}{\sqrt{2\pi\sigma^2}} \mathrm{e}^{i\theta} d\theta = \mathrm{e}^{-\sigma^2/2} = \mathrm{e}^{-D_\theta t}, \tag{54}$$

where D_θ is the diffusivity of the phase as calculated in section 7. Obviously from figure 9, the prediction (54) fails to describe the actual behavior of ε.

From our analysis of the strong dispersion limit, we know that as $\hbar \to \infty$, ε remains constant at the initial value of 1. This yields an interesting picture of the decay of the large scale energy as a function of $\hbar$. At $\hbar = 0$, the rate of decay of ε is faster than exponential. As $\hbar$ increases from 0, the rate of decay becomes faster than that for $\hbar = 0$. However, at some critical value of $\hbar > 1$, the rate of energy decay becomes slower than exponential and eventually becomes zero, since $\varepsilon = 1$ for all time as $\hbar \to \infty$.

11   Conclusion and Future Work

The main focus of the present study has been the attempt to understand some of the fundamental properties of the passive scalar dispersion equation (10) in the context of a random wave model (18) for the two dimensional background turbulent velocity field. We have found that the dispersivity parameter $\hbar$ greatly affects the spatiotemporal structure of the complex scalar A. For $\hbar = 0$, both the real and imaginary parts of A become highly stretched and contorted even after only 10 iterations of the random wave field. In contrast, for the case of $\hbar = 1$, the spatial structure of A looks blotchy with little indication of stretching or amplification of the gradient of A. As $\hbar$ increases, the time evolution of the spatial structure of A

18

becomes increasingly slower. Below a critical value $\hbar_c$, energy in the large scales of A decays faster than exponential; while for cases of $\hbar > \hbar_c$, the energy in the large scales decays slower than exponential. In fact, as $\hbar \to \infty$, the energy in the large scales remains constant at a value of unity. A useful extension of the present study would be to quantify the structure of A, visualized herein, using probability density functions. Another natural direction for future work would be to determine whether A exhibits a Batchelor scale. In other words, is there a limit to the smallest scales of A achievable in the flow? Additionally, if there is a cascade of energy from large to small scales, then what are the relevant scalings associated with the spectra and how do these compare with the case of passive scalar diffusion?

Finally with regard to near inertial oscillations, from the vertical normal mode decomposition presented in section 4 along with figure 2, we recognize that large $\hbar$ corresponds to low wavenumber vertical motions while $\hbar \to 0$ corresponds to high wavenumber vertical motions. It remains somewhat unclear, though, how one can directly apply the present observations regarding the variation in the decay of energy of A with $\hbar$ toward further understanding the behavior of the NIO velocity field in the oceanic mixed layer. Recall that in order to relate the NIO velocity field to the results of A presented here, we first need to compute $\mathcal{A}$ using the superposition of vertical normal modes and then apply the operator L. This is left as a task for future work.

12   Acknowledgments

13   Appendix

Here, we detail the integrations resulting from the Fourier series expansion of A as described in section 9. The corresponding terms in (47) will be referred to sequentially as $(\mathbf{I})$–$(\mathbf{V})$ starting from left to right. Each term is multiplied by $e^{-iqy-ipx}$ and integrated over $y = 0$–2π and $x = 0$–2π. Due to orthogonality of the Fourier modes,

$$\int_{x=0}^{2\pi} e^{i(k-p)x}dx = 2\pi\,\delta_{kp} \quad \text{and} \quad \int_{y=0}^{2\pi} e^{i(\ell-q)y}dy = 2\pi\,\delta_{\ell q}, \tag{55}$$

where δ is the kronecker delta. The two stages of the advection process are considered separately. We only outline integrations for the first stage; those for the second stage follow in a similar manner. The first advection stage occurs during time intervals, $2n\tau < t \le (2n+1)\tau$, $n = 0, 1, \ldots$ with the streamfunction given by $\Psi = \sin(y + \phi)$. Terms in (47), excluding term $(\mathbf{II})$ which is identically zero, are as follows:

$$\textbf{(I)} \quad \int_0^{2\pi} \left[\int_0^{2\pi} \sum_{k,\ell=-\infty}^{\infty} \dot{a}_{k,\ell}(t)\, e^{i(k-p)x} dx \right] e^{i(\ell-q)y} dy = (2\pi)^2 \dot{a}_{k,\ell},$$

$$\textbf{(III)} \quad -\int_0^{2\pi} \left[\int_0^{2\pi} \sum_{k,\ell=-\infty}^{\infty} ik\cos(y+\phi) a_{k,\ell}(t)\, e^{i(\ell-q)y} dy \right] e^{i(k-p)x} dx =$$

$$-\int_0^{2\pi} \left[\sum_{k=-\infty}^{\infty} i2\pi k \left(a_{k,\ell+1}(t)\frac{e^{-i\phi}}{2} + a_{k,\ell-1}\frac{e^{i\phi}}{2} \right) \right] e^{i(k-p)x} dx =$$

$$- ik(2\pi)^2 \left[a_{k,\ell+1}\left(\frac{e^{-i\phi}}{2} \right) + a_{k,\ell-1}\left(\frac{e^{i\phi}}{2} \right) \right],$$

$$\textbf{(IV)} \quad -\int_0^{2\pi} \left[\int_0^{2\pi} \frac{-i}{2}\sin(y+\phi) \sum_{k,\ell=-\infty}^{\infty} a_{k,\ell}(t)\, e^{i(\ell-q)y} dy \right] e^{i(k-p)x} dx =$$

$$-\int_0^{2\pi} 2\pi \left[\frac{e^{-i\phi}}{4} \sum_{k=-\infty}^{\infty} a_{k,\ell+1}(t) - \frac{e^{i\phi}}{4} \sum_{k=-\infty}^{\infty} a_{k,\ell-1}(t) \right] e^{i(k-p)x} dx =$$

$$(2\pi)^2 \left[a_{k,\ell+1}\left(\frac{e^{-i\phi}}{4} \right) - a_{k,\ell-1}\left(\frac{e^{i\phi}}{4} \right) \right],$$

$$\textbf{(V)} \quad \int_0^{2\pi} \left[\int_0^{2\pi} \frac{-i\hbar}{2} \sum_{k,\ell=-\infty}^{\infty} (k^2+\ell^2) a_{k,\ell}(t)\, e^{i(\ell-q)y} dy \right] e^{i(k-p)x} dx =$$

$$- (2\pi)^2 \frac{i\hbar}{2}(k^2+\ell^2) a_{k,\ell}(t).$$

Note, terms similar to $\cos(y+\phi)\, e^{i(\ell-q)y}$ can be easily integrated by rewriting the trigonometric part as an exponential, e.g. $1/2(e^{i(y+\phi)} + e^{-i(y+\phi)})$.

References

[1] E. A. D'Asaro, C. C. Eriksen, M. D. Levine, P. Niiler, C. A. Paulson, and P. Van Meurs, "Upper-ocean inertial currents forced by a strong storm. Part I: Data and comparison with linear theory," J. Phys. Ocean. **25**, 2909 (1995).

[2] W. R. Young and M. Ben Jelloul, "Propagation of near-inertial oscillations through geostrphic flow," J. Mar. Res. **55**, 735 (1997).

[3] N. J. Balmforth, S. G. Llewellyn Smith, and W. R. Young, "Enhanced dispersion of near-inertial waves in an idealized geostrophic flow," J. Mar. Res. **56**, 1 (1998).

[4] A. E. Gill, *Atmospher—Ocean Dynamics* (Academic Press, London, 1982).

[5] W. J. Emery, W. G. Lee, and L. Magaard, "Geographic and seasonal distributions of Brunt-Väisälä frequency and Rossby radii in the North Pacific and North Atlantic," J. Phys. Ocean. **14**, 294 (1984).

[6] A. E. Gill, "On the behavior of internal waves in the wakes of storms," J. Phys. Ocean. **14**, 1129 (1984).

[7] G. K. Batchelor, "Small-scale variation of convected quantities like temperature in turbulent fluid," J. Fluid Mech. **5**, 113 (1958).

[8] R. Pierrehumbert, "Tracer microstructure in the large-eddy dominated regime," Chaos, Solitons, and Fractals **4**, 1091 (1994).

[9] R. Seydel, *Practical bifurcation and stability analysis: from equilibrium to chaos* (Springer-Verlag, New York, 1994).

[10] S. Redner, "Random multiplicative processes: An elementary tutorial," American Journal of Physics **58**, 267 (1990).

[11] A. Einstein, "On the movement of small particles suspended in a stationary liquid demanded by the molecular kinetic theory of heat," Annalen der Physik **17**, 549 (1905).